

AN ABSTRACT OF THE THESIS OF

Paul W. Talbot for the degree of Master of Science in Nuclear Engineering presented on August 2012.

Title: Expanding the Discrete Maximum Principle for the IMC equations.

Abstract approved:

---

Todd S. Palmer

TODO

©Copyright by Paul W. Talbot  
August 2012  
All Rights Reserved

Expanding the Discrete Maximum Principle for the IMC equations

by

Paul W. Talbot

A THESIS

submitted to

Oregon State University

in partial fulfillment of  
the requirements for the  
degree of

Master of Science

Presented August 2012

Commencement August 2012

Master of Science thesis of Paul W. Talbot presented on August 2012.

APPROVED:

---

Major Professor, representing Nuclear Engineering

---

Head of the Department of Nuclear Engineering and Radiation Health Physics

---

Dean of the Graduate School

I understand that my thesis will become part of the permanent collection of Oregon State University libraries. My signature below authorizes release of my thesis to any reader upon request.

---

Paul W. Talbot, Author

# TABLE OF CONTENTS

	<u>Page</u>
1 Introduction . . . . .	9
1.1 Thermal Radiative Transfer . . . . .	9
1.2 Previous Research . . . . .	9
1.3 Research Objectives . . . . .	12
1.4 Outline . . . . .	12
2 Implicit Monte Carlo . . . . .	13
2.1 Thermal Radiative Transfer Equations . . . . .	13
2.2 Implicit Monte Carlo . . . . .	14
2.3 Discrete Maximum Principle . . . . .	16
3 Expansion of the Discrete Maximum Principle . . . . .	17
3.1 Introduction . . . . .	17
3.2 Non-Equilibrium Initial Conditions . . . . .	18
3.2.1 Uncollided Intensity . . . . .	21
3.2.2 Collided Intensity . . . . .	22
3.3 Analysis of $R$ . . . . .	26
3.3.1 Approximating $\tilde{R}$ . . . . .	26
3.3.2 Temperature . . . . .	27
3.3.3 Time Step . . . . .	28
3.3.4 Numerical Comparison . . . . .	28
3.4 Multiple Gradients . . . . .	31
3.5 Multidimensional Considerations . . . . .	35
3.6 Multigroup Frequencies . . . . .	36

## TABLE OF CONTENTS (Continued)

	<u>Page</u>
3.6.1 Riemann Approximation . . . . .	37
3.6.2 Accuracy of Multigroup Approximation . . . . .	38
3.6.3 Grey Case . . . . .	39
3.7 Summary . . . . .	42
4 Results . . . . .	43
4.1 Introduction . . . . .	43
4.2 Multigroup Treatment . . . . .	43
4.3 Non-Equilibrium Conditions . . . . .	45
4.4 Multiple Sources . . . . .	45
4.5 Small $\Delta T$ . . . . .	45
4.6 Summary . . . . .	49
5 Conclusions . . . . .	50
5.1 Future Work . . . . .	50

## LIST OF FIGURES

<u>Figure</u>		<u>Page</u>
1	$\lambda$ as a function of material temperature . . . . .	27
2	Energy Deposited, $R$ . . . . .	29
3	Absolute Error in $R$ Approximations . . . . .	30
4	Relative Error in $R$ Approximations . . . . .	30
5	Visualization of Riemann Sum Method . . . . .	38
6	Multigroup versus Analytic Solutions for the DMP . . . . .	39
7	Multigroup Approximation of DMP . . . . .	40
8	Marshak Wave in One Dimension . . . . .	44
9	Multiple Marshak Wave Sources . . . . .	46
10	Multiple Time Steps, Before Switch . . . . .	48
11	Multiple Time Steps, After Switch . . . . .	48





## 1 Introduction

### 1.1 Thermal Radiative Transfer

In general, three modes have been identified for heat transfer. Conduction occurs when two static materials are adjacent to each other, and convection involves one material moving with respect to another. The third mode, radiative heat transfer, is the result of photons generated by one material transporting to another and depositing some of their energy.

For energies typical to most terrestrial problems such as 0.026 eV (30 degrees Celsius), conduction and convection dominate heat transfer. At higher energies like  $10^3$  eV (11 million degrees Celsius), as suggested by blackbody photon emission dependence on temperature, radiation becomes more important and can be the dominant form of heat transfer. These kinds of extreme temperatures occur in many situations of interest, including fusion reactor startup and operation and celestial events such as supernovas.

### 1.2 Previous Research

In 1971, workers at the then-named Lawrence Radiation Laboratory proposed a new method for Monte Carlo treatment of the radiative heat transport equations, particularly targeting optically thick systems [4]. As they pointed out, several attempts at applying Monte Carlo to the very nonlinear radiative heat transfer equations, but they were successful only largely for optically thin problems [5]. Fleck and Cummings' method served to semi-implicitly treat the radiative heat transfer equations, although, as they pointed out, some overheating occurred in certain choices of time and spatial steps, which is the focus of this work. This method became commonly known as implicit Monte Carlo (IMC).

While the IMC method quickly gained traction in radiative transport solutions, the undesirable instability depending on time and spatial step size led Larsen and Mercier to construct a maximum principle based on assuming temporal discretization. While they did obtain a bounding equation for time step size, it proved very conservative, to the point of being impractical.

More recently, Jeff Densmore and Ed Larsen [6] performed an asymptotic study on several Monte Carlo approaches to the radiative heat transfer equations: the Carter-Forest [8], N’Kaoua [11], and Fleck and Cummings. Since Fleck and Cummings’ IMC approach is fundamental to this work, their findings are of interest. In particular, Densmore and Larsen sought to test the equilibrium diffusion limit of the IMC method, meaning in an asymptotic analysis of the equations results in “an accurate, time-discretized version of the equilibrium diffusion equation,” then accurate solutions should be generated given an appropriate choice of time discretization. They found that the IMC method did not have this limit, further highlighting the difficulties between temporal and spatial discretization and accurate solutions for the IMC equations.

Other attempts have also been made recently to find improved methods for radiative heat transfer. At Los Alamos National Laboratory, Densmore, Urbatsch, Evans, and Buksas proposed a hybrid method using transport and diffusion called the Discrete Diffusion Monte Carlo (DDMC) [7]. Particularly for diffusive problems, the number of interactions lead to a large number of small time steps in order to accurately capture the physics of the problem. As with many hybrid methods, DDMC makes use of simplified diffusion solutions in regions within the mesh, replacing significant Monte Carlo particle tracking. Also, the hybrid method switches between Monte Carlo transport in optically thin areas and the diffusion

method for thick ones. This provides another great tool in solving a variety of radiative heat transfer problems.

Another attempt to improve the IMC method involved adding an adaptive adjustment to the definition of the Fleck factor by McClarren and Urbatsch. In general the Fleck factor includes a manually-selected  $\alpha$  term, which is set to either 1/2 or 1. McClarren shows how with slight redefinition of the Fleck factor, the IMC equations can result in less overheating. We will make use of his developments in this work.

A masters thesis from Oregon State University [10] concurrent with this work explored the possibility of using “sub-time steps” to update the temperature in a cell several times based on a small number of Monte Carlo particle runs in order to mitigate the overheating explored by Fleck and Cummings [4], Larsen and Mercier [9], and Wollaber, Larsen, and Densmore [13]. This development proved effective at reducing overheating, and has an intriguing possibility of being combined with the present work to adaptively allow a code to correct for potential overheating problems.

Most recently, researchers at Los Alamos National Laboratory have developed a discrete maximum principle [13], addressing the discrepancy between theory and practice brought up in [9]. In addition to assuming temporal discretization, they included spatial discretization to develop an estimate for energy deposited in a cell as a function of space and time steps, which is then incorporated into a discrete maximum principle governing the maximum time step that will result in physically viable results for the problem. This discrete maximum principle (DMP) was demonstrated on a 1-dimensional Marshak wave problem, using a script separate from the simulation code. This DMP resulted in a bounding  $\Delta_x, \Delta_t$  curve that

closely matched experimental results.

### 1.3 Research Objectives

The objective of this work is threefold.

First, we adapt the existing DMP to use multifrequency approximations. Because the previous implementation of the DMP used existing semi-analytic tools built into third-party codes, these approximations will demonstrate that the DMP can be implemented directly into a wider variety of use codes.

Second, we remove the assumption of material and radiation field equilibrium initial conditions. This change only requires a small adjustment to existing terms, and allows the DMP to apply to a wider variety of physical systems.

Third, we demonstrate that, assuming linear superposition of energy deposition, the DMP can be modified to consider temperature gradients across all boundaries of a cell instead of just the largest gradient. While the existing method is excellent for single-dimension Marshak wave problems, this superposition assumption will allow a wider variety of problems to be protected by the DMP.

Lastly, we show that none of these adjustment impair the operation of the DMP, and the DMP algorithm continues to predict overheating for a wide variety of problems.

### 1.4 Outline

TODO

## 2 Implicit Monte Carlo

### 2.1 Thermal Radiative Transfer Equations

The thermal radiative transfer equations center around the generation, interaction, and absorption of photons in a background medium with non-zero temperature. The generation of photons by a material is described by Planck's blackbody distribution. For a given material temperature  $T$ , the spectrum of emitted photons by that material is given by

$$B(T) = \frac{2h\nu^3}{c^2} \frac{1}{\exp(\frac{h\nu}{kT}) - 1}, \quad (1)$$

where  $h$  is Planck's constant,  $\nu$  is photon frequency,  $c$  is the speed of light in a vacuum, and  $k$  is Boltzmann's constant. The interactions of photons with a background medium is represented by coupled integro-differential equations:

$$\frac{1}{c} \frac{\partial I}{\partial t}(\mathbf{r}, \boldsymbol{\Omega}, \nu, t) + \boldsymbol{\Omega} \cdot \nabla I(\mathbf{r}, \boldsymbol{\Omega}, \nu, t) = \sigma_a(\mathbf{r}, \boldsymbol{\Omega}, t) [B(\nu, T) - I(\mathbf{r}, \boldsymbol{\Omega}, \nu, t)], \quad (2a)$$

$$c_v(\mathbf{r}, T) \frac{\partial T}{\partial t}(\mathbf{r}, t) = \int_0^\infty \int_0^{4\pi} \sigma_a(\mathbf{r}, \nu', T) [(I(\mathbf{r}, \boldsymbol{\Omega}', \nu', t) - B(\nu', T))] d\boldsymbol{\Omega}' d\nu', \quad (2b)$$

where  $I$  is the photon intensity,  $\sigma_a$  is the absorption opacity,  $c_v$  is the material heat capacity, and  $T$  is the material temperature.  $I$  is more accurately the photon intensity per second, here given in units of photons per  $\text{cm}^2$  per second. The opacity is similar to a macroscopic cross-section, with units of inverse centimeters.  $1/\sigma_a$  is the mean free path for a photon, or the average distance a photon with a given energy travels before being absorbed in the material.

The phase space considered for  $I$  covers particles at location  $\mathbf{r}$  in three-dimensional space, moving in solid angle  $\boldsymbol{\Omega}$ , with frequency  $\nu$ , all at time  $t$ .

## 2.2 Implicit Monte Carlo

While a complete derivation of the IMC method for radiative heat transfer is contained in previous work [4], here we repeat the single-frequency (grey) one-dimension derivation that leads to the Fleck factor.

We begin by taking Eqs. 2, assuming local thermodynamic equilibrium:

$$\frac{1}{c} \frac{\partial I}{\partial t} + \mu \frac{\partial I}{\partial x} + \sigma I = \frac{1}{2} \sigma_a a c T^4, \quad (3a)$$

$$c_v \frac{\partial T}{\partial t} - \sigma_a \left( \int_{-1}^1 I d\mu - a c T^4 \right), \quad (3b)$$

noting

$$\int_0^\infty B(\nu, T) d\nu = a c T^4. \quad (4)$$

Following after the fashion of Fleck and Cummings, we define

$$u_m = c_v T, \text{ material energy density,} \quad (5)$$

$$u_r = a T^4, \text{ radiation energy density,} \quad (6)$$

and

$$\frac{1}{\beta} = \frac{u_r}{u_m}. \quad (7)$$

Rewriting Eqs. 3,

$$\frac{1}{c} \frac{\partial I}{\partial t} + \mu \frac{\partial I}{\partial x} + \sigma_a I = \frac{1}{2} \sigma_a c u_r, \quad (8a)$$

$$\frac{\partial u_r}{\partial t} = \beta \sigma \left( \int_{-1}^1 I d\mu - c u_r \right). \quad (8b)$$

We then begin discretizing by integrating over time  $t = t^n$  to  $t = t^{n+1}$ :

$$u_r^{n+1} - u_r^n = \int_{t^n}^{t^{n+1}} dt \beta \sigma \int_{-1}^1 I d\mu - c \int_{t^n}^{t^{n+1}} dt \beta \sigma u_r, \quad (9)$$

noting that

$$u_r^n = u_r(x, t^n).$$

Allowing  $\beta$  and  $\sigma$  to take a single average value over the time step and defining  $\Delta_t = t^{n+1} - t^n$ ,

$$u_r^{n+1} - u_r^n = \Delta_t \beta \sigma \left\{ \int I d\mu - c[\alpha u_r^{n+1} + (1 - \alpha)u_r^n] \right\}, \quad (10)$$

where  $\alpha$  ranges between 0 and 1 and determines the implicitness of the radiation energy densities. In practice,  $\alpha$  usually takes the value of 1/2 or 1, with strong preference being given to  $\alpha = 1$  for stability, although adaptive methods for selecting  $\alpha$  have been proposed [12]. We have also assumed an appropriate value for  $I$  has been determined for the time step by some centering, implicit, or explicit method. For this derivation, we may assume an instantaneous value is representative of the value throughout the time step. Solving for  $u_r^{n+1}$ ,

$$u_r^{n+1} = \frac{1 - (1 - \alpha)\beta c \Delta_t \sigma}{1 + \alpha\beta c \Delta_t \sigma} u_r^n + \frac{\beta \sigma \Delta_t}{1 + \alpha\beta c \Delta_t \sigma} \int I d\mu. \quad (11)$$

Defining  $u_r = \alpha u_r^{n+1} + (1 - \alpha)u_r^n$ , then solving Eq. 11 for  $u_r$  and plugging into Eq. 8a yields

$$\frac{1}{c} \frac{\partial I}{\partial t} + \mu \frac{\partial I}{\partial x} + \sigma I = \frac{1}{2} \sigma \left( \frac{\alpha\beta c \Delta_t \sigma}{1 + \alpha\beta c \Delta_t \sigma} \right) \int I d\mu + \frac{1}{2} \left( \frac{c\sigma u_r^n}{1 + \alpha\beta c \Delta_t \sigma} \right). \quad (12)$$

This brings us to the Fleck factor  $f$ , which we define as

$$f = \frac{1}{1 + \alpha\beta c \Delta_t \sigma}, \quad (13)$$

and we may write the thermal radiative transfer equations as

$$\frac{1}{c} \frac{\partial I}{\partial t} + \mu \frac{\partial I}{\partial x} + \sigma_a I = \frac{\sigma(1 - f)}{2} \int I d\mu + \frac{f c \sigma u_r^n}{2}, \quad (14a)$$

$$c_v \frac{\partial T}{\partial t} = \sigma f \int_{\Delta_t} \int_{-1}^1 I d\mu dt - f(c \Delta_t \sigma u_r^n). \quad (14b)$$

A similar derivation for the multifrequency case (see [4]) leads to radiative thermal transfer equations of a similar form:

$$\frac{1}{c} \frac{\partial I}{\partial t} + \mu \frac{\partial I}{\partial x} + \sigma I = \frac{1 - f}{2} \frac{\sigma b}{\sigma_p} \int_0^\infty \int_{-1}^1 \sigma I d\mu d\nu + \sigma f 2\pi B, \quad (15a)$$

$$c_v \frac{\partial T}{\partial t} = f \int_0^\infty \int_{-1}^1 \sigma(I - 2\pi B) d\mu d\nu, \quad (15b)$$

where we introduce

$$\sigma_p = \int_0^\infty b \sigma d\nu, \quad (16)$$

and  $b$  is the integrated Planck spectrum.

### 2.3 Discrete Maximum Principle

TODO parrot DMP derivation



### 3 Expansion of the Discrete Maximum Principle

#### 3.1 Introduction

The findings presented in this work center around four major adjustments to the DMP: removing an equilibrium assumption, reducing the complexity of the estimated deposited energy, handling multiple temperature gradients on a single cell's boundaries, and applying multigroup frequency approximations.

One of the assumptions originally made in [13] is initial equilibrium between the material and radiation temperatures at the start of each time step. While this is physically reasonable in most circumstances, we consider the DMP more flexible if this assumption is removed.

The term  $R$ , signifying the estimated energy deposited in a cell over a time step from neighboring cells, exists in previous work as a almost-unmanagably large term involving a combination of operators and integrals. Because the DMP is intended to be used as a predictive warning for existing use codes, it is critical that the prediction does not significantly slow the overall problem simulation. This makes reducing  $R$  to a more manageable, code-friendly set of terms desirable. We will analyze the components of  $R$  and approximate  $R$  by removing components that do not significantly effect its value over a wide range of time and spatial steps.

In previous work, the DMP was only applied to a one-dimensional Marshak wave problem, where a single source impinged on a single side of the material. While this has been effective to demonstrate the predicting capacity of the DMP, it is conceivable that a simulation involving two hot cells bordering a cold cell may result in a violation of the maximum principle, even when neither hot cell might produce a violation independently. We will assume linear superposition of energy

deposition to derive a multiple-dimension adjustment that improves predictive capacity of the DMP.

Lastly, previous computation of the DMP has involved using a semi-analytic integration routine. As part of integrating the DMP into use code, we find it prudent to adapt the DMP to rely on multigroup frequency approximations similar to those used in the implicit Monte Carlo solver itself. As we will show, this approximation not only makes the DMP easier to implement, but also reduces computation time and increases predictive accuracy.

### 3.2 Non-Equilibrium Initial Conditions

Parallel to the derivation performed in [13], we consider a single time step, for instance the first step  $0 \leq t \leq t_1$ . All future time steps  $t_n \leq t \leq t_{n+1}$  can be treated in a similar fashion. Opacity and specific heat are treated explicitly at  $t = 0$  as  $\sigma_0$  and  $c_{v0}$  respectively. We retain the definitions from [13]:

$$B(\nu, T) = \text{Planck spectrum} = \frac{15ac}{4\pi^5} \frac{\nu^3}{e^{\nu/T} - 1}, \quad (17a)$$

$$b(\nu, T) = \text{normalized Plank spectrum} = \frac{15}{\pi^4 T^4} \frac{\nu^3}{e^{\nu/T} - 1}, \quad (17b)$$

$$\sigma(\nu, T) = \text{absorption opacity} = \frac{\gamma}{\nu^3} (1 - e^{-\nu/T}), \quad (17c)$$

$$\sigma_p = \int_0^\infty b(\nu, T_0) \sigma(\nu, T_0) d\nu = \frac{15\gamma}{\pi^4 T_0^3}, \quad (17d)$$

$$f_0 = \text{Fleck factor} = \frac{1}{1 + \beta_0 \sigma_0 c \Delta_t}, \quad (17e)$$

$$\beta_0 = \frac{\partial a T_0^4 / \partial T}{\partial c_{v0} T_0 / \partial T} = \frac{4a T_0^3}{c_{v0}}, \quad (17f)$$

$$a = \text{radiation constant} = 0.01372 \frac{\text{jk}}{\text{cm}^3 \text{keV}^4}, \quad (17g)$$

$$c = \text{speed of light} = 299.792458 \text{cm / sh.} \quad (17h)$$

With Eqs. (17) defined and moving to a 1-dimensional geometry in the  $x$ -direction, Eqs. (2a) and (2b) take the following form, dropping dependency notation:

$$\frac{1}{c} \frac{\partial I}{\partial t} + \mu \frac{\partial I}{\partial x} + \sigma I = \frac{1 - f_0}{2} \frac{\sigma_0 b_0}{\sigma_p} \int_0^\infty \int_{-1}^1 \sigma_0 I \, d\mu \, d\nu + \sigma_0 f_0 2\pi B_0,$$

$$0 \leq x \leq \infty, \quad |\mu| \leq 1, \quad 0 \leq t \leq t_1, \quad (18a)$$

$$\frac{c_{v0}}{\Delta_t} (T_1 - T_0) = \frac{f_0}{\Delta_t} \int_0^{\Delta_t} \int_0^\infty \int_{-1}^1 \sigma_0 (I - 2\pi B_0) \, d\mu \, d\nu \, dt. \quad (18b)$$

The initial and boundary conditions are given by:

$$I(0, \mu, \nu, t) = 2\pi B_u \equiv 2\pi B(\nu, T_u), \quad 0 < \mu \leq 1, \quad 0 \leq t, \quad (18c)$$

$$I(\infty, \mu, \nu, t) = 2\pi B_0 \equiv 2\pi B(\nu, T_0), \quad -1 \leq \mu \leq 1, \quad 0 \leq t, \quad (18d)$$

$$I(x, \mu, \nu, 0) = I_i, \quad 0 \leq x \leq \infty, |\mu| < 1. \quad (18e)$$

Eq. (18e) is the first deviation from [13], where the initial intensity was set to the same properties as the right boundary condition, which assumes complete thermal equilibrium.

We spatially discretize Eqs. (18) into  $J$  distinct portions, or grid cells, each with a left boundary at  $x_j$  and having width  $\Delta_{x,j} = x_{j+1} - x_j$ . The average temperature within each cell is given by a temperature averaging function:

$$T_j = \frac{1}{\Delta_{x,j}} \int_{x_j}^{x_{j+1}} T(x) dx, \quad 0 \leq j \leq J-1.$$

In this manner, the discontinuous temperature approximation function  $\tilde{T}(x)$  approximates the physical continuous temperature function  $T(x)$  as follows:

$$\tilde{T}(x) \equiv \sum_{j=0}^{J-1} \chi_j(x) T_j \approx T(x),$$

where  $\chi_j$  is a piecewise distribution, as follows:

$$\chi_j(x) \equiv \begin{cases} 1 & x_j \leq x \leq x_{j+1}, \\ 0 & \text{otherwise.} \end{cases} \quad (19)$$

Thus, temperature is often treated in as piecewise constant by using  $\tilde{T}(x)$  instead of  $T(x)$  for explicit terms in Eqs. (18) such as  $\sigma$  and  $B$ . The material equation then appears as follows:

$$\frac{\tilde{c}_{v0}}{\Delta_t} (T_{j,1} - T_{j,0}) + \tilde{f}_0 \tilde{\sigma}_p a c T_{j,0}^4 = \frac{\tilde{f}_0}{\Delta_{x,j} \Delta_t} \int_0^\infty \tilde{\sigma}_0 \int_{x_j}^{x_{j+1}} \int_{\Delta_t} \int_{-1}^1 I d\mu dt dx d\nu. \quad (20)$$

The previous definitions, time-explicit coefficients, and grid data are typical for the IMC equations. In the following sections, we introduce additional approximations in order to estimate the radiation energy deposited in the first cell. We start by assuming separability of the radiative intensity  $I$  into the collided ( $\check{I}$ ) and uncollided ( $\hat{I}$ ) parts so that  $\hat{I} + \check{I} = I$ .

### 3.2.1 Uncollided Intensity

We approach the uncollided intensity first because it is more analytically tractable and appears in the collided intensity equation as a source term. The following equations govern uncollided intensity:

$$\frac{1}{c} \frac{\partial \hat{I}}{\partial t} + \mu \frac{\partial \hat{I}}{\partial x} + \sigma_0 \hat{I} = 0, \quad (21a)$$

$$\hat{I}(0, \mu, \nu, t) = 2\pi B_u, \quad 0 < \mu \leq 1, \quad 0 \leq t, \quad (21b)$$

$$\hat{I}(\infty, \mu, \nu, t) = 0, \quad -1 \leq \mu < 0, \quad 0 \leq t, \quad (21c)$$

$$\hat{I}(x, \mu, \nu, 0) = 0, \quad 0 \leq x \leq \infty, \quad |\mu| \leq 1. \quad (21d)$$

Given the lack of any source terms in Eqs. (21), the system is completely absorbing in nature. It could be solved analytically, but will be treated by discretizing in time implicitly:

$$\frac{1}{c} \left( \frac{\hat{I}_1 - \hat{I}_0}{\Delta t} \right) + \mu \frac{\partial}{\partial x} \hat{I}_1 + \sigma_0 \hat{I}_1 = 0,$$

where  $\hat{I}_k \equiv \hat{I}(t_k)$  designates the uncollided radiation intensity at discrete time step  $t_k$ . Because of the specified initial condition (i.e., all intensity existing at the start of the problem is collided intensity, the uncollided intensity is zero throughout the mesh at time  $t = 0$ ),

$$\frac{1}{c\Delta t} \hat{I}_1 + \mu \frac{\partial}{\partial x} \hat{I}_1 + \sigma_0 \hat{I}_1 = 0,$$

or, in operator form,

$$\mu \frac{\partial \hat{I}_1}{\partial x} + \left( \sigma_0 + \frac{1}{c\Delta t} \right) \hat{I}_1 = 0. \quad (22)$$

For  $\mu \geq 0$  the solution for the time-implicit uncollided radiation is found using the integrating factor  $e^{\sigma_0 x + \frac{1}{c\Delta t} x} \equiv e^{\hat{\Sigma}(\nu)x}$ :

$$\hat{I}_1(x, \mu, \nu) = 2\pi B_u e^{-\hat{\Sigma}x/\mu}. \quad (23)$$

This is limited to particles traveling in angles of positive  $\mu$ . This is practical for a problem with isotropically impinging radiation on once face of a cell; however, further treatment is necessary in order to account for significant influences on multiple faces of a cell. This will be addressed in Section ?? for both single- and multidimensional cases.

Taking the zeroth angular moment of Eq. (23),

$$\begin{aligned}\hat{\phi}_1(x, \nu) &\equiv \int_{-1}^1 \hat{I}_1 d\mu = \int_0^1 2\pi B_u e^{-\hat{\Sigma}x/\mu} d\mu, \\ \hat{\phi}_1(x, \nu) &= 2\pi B_u E_2(\hat{\Sigma}x).\end{aligned}\tag{24}$$

where  $E_n$  is the exponential integral defined as follows:

$$E_n(x) \equiv \int_0^1 \mu^{n-2} e^{-x/\mu} d\mu, \quad 0 < x.$$

Eq. (24), is the approximate solution of the uncollided intensity. Note that this derivation coincides precisely with the process employed by Wollaber, Larsen, and Densmore [13].

### 3.2.2 Collided Intensity

It is in this section that the deviation from previous derivation of the discrete maximum principle occurs. Because the collided intensity contains all the source terms, it is more difficult to treat. Eqs. (25) are the governing equations of the collided intensity:

$$\frac{1}{c} \frac{\partial \check{I}}{\partial t} + \mu \frac{\partial \check{I}}{\partial x} + \sigma_0 \check{I} = \frac{1 - f_0}{2} \frac{\sigma_0 b_0}{\sigma_p} \int_0^\infty \int_{-1}^1 \sigma_0 (\hat{I} + \check{I}) d\mu d\nu + 2\pi \sigma_0 f_0 B_0, \tag{25a}$$

$$\check{I}(0, \mu, \nu, t) = 0, \quad 0 < \mu \leq 1, \quad 0 \leq t, \quad (25b)$$

$$\check{I}(\infty, \mu, \nu, t) = 2\pi B_R, \quad -1 \leq \mu < 0, \quad 0 \leq t, \quad (25c)$$

$$\check{I}(x, \mu, \nu, 0) = I_i(x, \mu, \nu), \quad 0 \leq x \leq \infty, \quad |\mu| \leq 1. \quad (25d)$$

Note that Eq. (25d) is the general initial condition employed particular to this derivation.

To solve Eqs. (25), a standard diffusion approximation is made, leading to the following:

$$\frac{1}{c} \frac{\partial \check{\phi}}{\partial t} - \frac{1}{3\sigma_0} \frac{\partial^2 \check{\phi}}{\partial x^2} + \sigma_0 \check{\phi} = (1 - f_0) \frac{\sigma_0 b_0}{\sigma_p} \int_0^\infty \sigma_0 (\hat{\phi} + \check{\phi}) d\nu + 4\pi f_0 \sigma_0 B_0, \quad (26)$$

where the scalar intensity  $\check{\phi}$  is

$$\check{\phi}(x, \nu, t) \equiv \int_{-1}^1 \check{I}(x, \mu, \nu, t) d\mu.$$

As in [13], it is assumed that  $\check{\phi}$  has a frequency shape given by the Planckian spectrum  $b_0$  for cell temperature  $T_0$ , allowing it to be separated as follows:

$$\check{\phi}(x, \nu, t) \approx b_0(\nu) \check{\phi}(x, t).$$

Defining the diffusion coefficient

$$D \equiv \int_0^\infty \frac{b_0(\nu)}{3\sigma_0(\nu)} d\nu, \quad (27)$$

Eq. (26) can be integrated over all frequencies  $\nu$  to obtain

$$\frac{1}{c} \frac{\partial \check{\phi}}{\partial t} - D \frac{\partial^2 \check{\phi}}{\partial x^2} + f_0 \sigma_p \check{\phi} = (1 - f_0) \int_0^\infty \sigma_0 \hat{\phi} d\nu + f_0 \sigma_p a c T_0^4. \quad (28)$$

At this point, an implicit time discretization is employed, although the approach is more general here given the undefined initial condition throughout the mesh

given in Eqs. (25). Implicit time discretization is employed as follows for any time-dependent function  $f(t)$ :

$$\bar{f}(t) \equiv \frac{1}{\Delta_t} \int_{t_n}^{t_{n+1}} f(t) dt \approx f(t_{n+1}).$$

Additionally, we define the radiation temperature at time  $t = 0$  to satisfy:

$$\int_0^\infty \check{\phi}_0 d\nu \equiv \int_0^\infty \int_{-1}^1 \check{I}_i d\mu d\nu \equiv acT_R^4,$$

where we define  $T_R$  as the radiation field temperature within the cell at time  $t = 0$ .

Applying time differencing to Eq. (28), we arrive at the following:

$$\frac{\partial^2 \check{\phi}_1}{\partial x^2} - \lambda^2 \check{\phi}_1 = \frac{1 - f_0}{-D} \int_0^\infty \sigma_0 \hat{\phi} d\nu - \frac{acT_R^4}{c\Delta_t D} - \frac{f_0 \sigma_p}{D} acT_0^4, \quad (29)$$

where  $\lambda$  has been introduced as

$$\lambda^2 \equiv \frac{f_0 \sigma_p + 1/c\Delta_t}{D}.$$

Using Eq. (24) in Eq. (28),

$$\frac{\partial^2 \check{\phi}_1}{\partial x^2} - \lambda^2 \check{\phi}_1 = \frac{1 - f_0}{-D} \int_0^\infty \sigma_0 2\pi B_u E_2(\hat{\Sigma}x) d\nu - \frac{acT_R^4}{c\Delta_t D} - \frac{f_0 \sigma_p}{D} acT_0^4. \quad (30a)$$

As with [13], a Marshak boundary condition is set at the left:

$$\check{\phi}_1(0) - 2D \frac{d\check{\phi}_1}{dx} \Big|_{x=0} = 0, \quad (30b)$$

and the right boundary is

$$\lim_{x \rightarrow \infty} \check{\phi}_1(x) = acT_R^4. \quad (30c)$$

To bring this derivation back in harmony with [13],  $\tilde{A}$  is defined

$$\tilde{A} \equiv -\frac{acT_R^4}{c\Delta_t D} - \frac{f_0 \sigma_p}{D} acT_0^4, \quad (30d)$$

and operator  $L$

$$L(\xi) \equiv \frac{1 - f_0}{-D} \int_0^\infty \sigma_0 2\pi B_u \xi d\nu, \quad (30e)$$



making Eq. (30f), the simplification of Eq. (30a), identical in appearance to Eq. (17g) in [13]:

$$\frac{\partial^2 \check{\phi}_1}{\partial x^2} - \lambda^2 \check{\phi}_1 = \tilde{A} + L \left( E_2(\hat{\Sigma}x) \right). \quad (30f)$$

We see by inspection that the remainder of the derivation in [13] applies perfectly to (30f), only trivially replacing  $A$  everywhere with  $\tilde{A}$ . The final results arrived at in [13] are shown here, noting only that  $\tilde{R}$  (the average energy deposited in the first cell) and  $\tilde{A}$  contain the radiation temperature  $T_R$  as well as the material temperature  $T_0$ .

$$\begin{aligned} \tilde{R}(\Delta_x, \Delta_t) \equiv & \frac{f_0 \Delta_t 2\pi}{\Delta_x} \int_0^\infty \frac{\sigma_0 B_u}{\hat{\Sigma}} \left( \frac{1}{2} - E_3(\hat{\Sigma} \Delta_x) \right) d\nu \\ & + \frac{c_1 f_0 \Delta_t \sigma_p}{\lambda \Delta_x} (1 - e^{-\lambda \Delta_x}) + \frac{f_0 \Delta_t \sigma_p}{\lambda^2 \Delta_x} \left[ -\tilde{A} \Delta_x - L \left\{ \frac{1}{\hat{\Sigma}} \left( \frac{1}{2} - E_3(\hat{\Sigma} \Delta_x) \right) \right\} \right] \\ & + \frac{f_0 \Delta_t \sigma_p}{\Delta_x \lambda^4} L \left\{ \hat{\Sigma} \left[ e^{-\lambda \Delta_x} \text{Ei}[(\lambda - \hat{\Sigma}) \Delta_x] + e^{\lambda \Delta_x} \text{Ei}[-(\lambda + \hat{\Sigma}) \Delta_x] \right. \right. \\ & \left. \left. - 2 \text{Ei}(-\hat{\Sigma} \Delta_x) + \ln \frac{\hat{\Sigma}^2}{(\lambda + \hat{\Sigma})|\lambda - \hat{\Sigma}|} \right] \right\}, \end{aligned} \quad (31)$$

Thus, the IMC equations can be expected to satisfy the maximum principle if the following inequality is satisfied, calculating  $\tilde{R}$  as in Eq. (31).

$$\Delta_t < \frac{c_v (T_u - T_0)}{\tilde{R}(\Delta_x, \Delta_t) - f_0 c \sigma_p a T_0^4}. \quad (32)$$

Eq. (32) represents the DMP without assuming initial equilibrium between the radiation and material temperatures.

### 3.3 Analysis of $R$

Continuing from Eq. (32), we seek a functional form more agreeable for use in a coding environment. Primarily, this involves approximating computationally difficult functions such as the exponential integrals  $E_n(x)$  and  $\text{Ei}(x)$ , as well as numerically evaluating the various integrals over frequency.

#### 3.3.1 Approximating $\tilde{R}$

We address each of the terms of  $\tilde{R}$  by breaking them up in Eq. (33):

$$\tilde{R}(\Delta_x, \Delta_t) \equiv \frac{f_0 \Delta_t 2\pi}{\Delta_x} \int_0^\infty \frac{\sigma_0 B_u}{\hat{\Sigma}} \left( \frac{1}{2} - E_3(\hat{\Sigma} \Delta_x) \right) d\nu \quad (33a)$$

$$+ \frac{c_1 f_0 \Delta_t \sigma_p}{\lambda \Delta_x} (1 - e^{-\lambda \Delta_x}) \quad (33b)$$

$$+ \frac{f_0 \Delta_t \sigma_p}{\lambda^2 \Delta_x} \left[ -\tilde{A} \Delta_x - L \frac{1}{\hat{\Sigma}} \left( \frac{1}{2} - E_3(\hat{\Sigma} \Delta_x) \right) \right] \quad (33c)$$

$$+ \frac{f_0 \Delta_t \sigma_p L}{\Delta_x \lambda^4} \hat{\Sigma} \left[ e^{-\lambda \Delta_x} \text{Ei}[(\lambda - \hat{\Sigma}) \Delta_x] + e^{\lambda \Delta_x} \text{Ei}[-(\lambda + \hat{\Sigma}) \Delta_x] \right. \\ \left. - 2 \text{Ei}(-\hat{\Sigma} \Delta_x) + \ln \frac{\hat{\Sigma}^2}{(\lambda + \hat{\Sigma})|\lambda - \hat{\Sigma}|} \right]. \quad (33d)$$

While the terms in Eq. (33) are generally listed in order of increasing powers of  $\lambda$  in the denominator, it should be noted that term (33b) actually contains the term  $\lambda^4$ , because of the definition of  $c_1$  in Eq. (31) of [13]:

$$c_1 = \frac{1}{1 + 2D\lambda} \frac{1}{\lambda^2} \left[ A + L \left( 1 + \frac{\hat{\Sigma}}{2\lambda} \ln \frac{|\lambda - \hat{\Sigma}|}{\lambda + \hat{\Sigma}} \right) \right], \quad \lambda \neq \hat{\Sigma}.$$

Inspection of the definition of  $\lambda$  (repeated below) assists in assigning the relative importance of terms in Eq. (33):

$$\lambda^2 \equiv \frac{f_0 \sigma_p + 1/c \Delta_t}{D} = \frac{f_0 \sigma_p}{D} + \frac{1}{Dc \Delta_t}$$

Since  $f_0$  is restricted from zero to one, primary attention is turned to the other terms in  $\lambda^2$ .

### 3.3.2 Temperature

Figure 1 shows  $\lambda^2$  versus temperature for constants  $\gamma = 27 \text{ keV}^3/\text{cm}$ ,  $c = 3 \times 10^2 \text{ cm/sh}$ , and  $\Delta_t = 10^{-5} \text{ sh}$ . Additionally, it is assumed that the Planck opacity has the functional form

$$\sigma_p = \frac{15\gamma}{\pi^4 T_0^3}, \quad (34)$$

which may not be valid for many real materials, but serves as a physically viable test case.

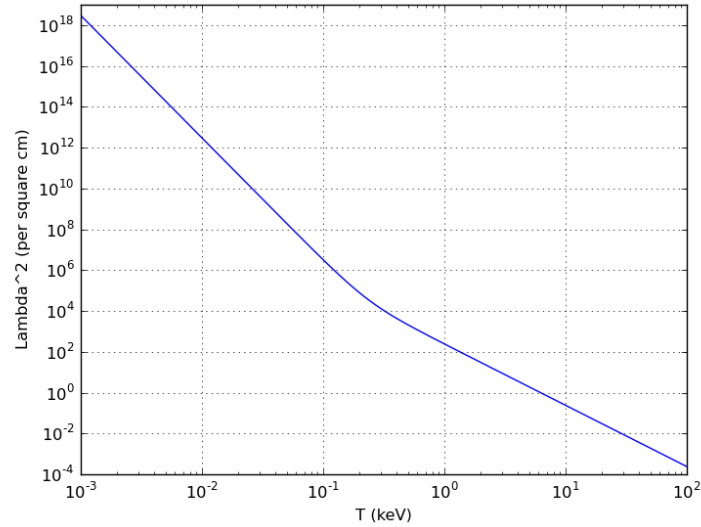


Figure 1:  $\lambda$  as a function of material temperature

As can be seen,  $\lambda^2$  falls as  $T^6$  until an inflection point is reached near  $T = 0.3 \text{ keV}$ , after which it falls as  $T^3$ . It is worth noting that for most of the range  $0 < T < 1 \text{ keV}$ ,  $\lambda^2$  is very large. As such, terms in  $\tilde{R}$  with exponential values of  $\lambda^2$  will be vanishingly small for most temperatures below 1 keV; however, further analysis

needs to be done in order to determine how many terms in  $\tilde{R}$  can be neglected because of their insignificance next to other terms because of temperature.

### 3.3.3 Time Step

It is also enlightening to consider the effect of an increasing time step on  $\lambda^2$ . Since a  $1/\Delta_t$  term is in the numerator of  $\lambda^2$ , a term with  $1/\lambda^2$  varies as  $O(\Delta_t)$  as  $\Delta_t \rightarrow \infty$ . In Eq. (33), a  $\Delta_t$  term already exists in the numerator of each term. Thus, term (33a) varies linearly with  $\Delta_t$ . The term with the next lowest order of  $\lambda$ , term (33c), has a  $1/\lambda^2$  coefficient, meaning it varies as  $\Delta_t^2$ . Terms (33b) and (33d) vary as  $\Delta_t^{5/2}$  and  $\Delta_t^3$  respectively. Thus, as the time step becomes large, the latter terms in Eq. (33) become more significant.

It is unclear from the influence of both  $T$  and  $\Delta_t$  what terms in  $\tilde{R}$  are necessary to maintain accuracy for a variety of conditions. Future work will be done to evaluate these terms independently in the limit as  $\Delta_t \rightarrow 0, \infty$ . For the sake of the current work, we turn to numerical methods to evaluate the relative impact of the terms, acknowledging the results are specific to this particular sample problem.

### 3.3.4 Numerical Comparison

Given the difficulty in analytically determining the importance of the terms in  $\tilde{R}$ , we performed a numerical study similar to that in [13], using the same values for  $\sigma_p$ ,  $\beta$ , and  $D$ . In each run, one of the terms in Eq. (33) was set to zero, with the exception of the first term, which is the dominant contributor to  $\tilde{R}$  for this problem. Instead, the first term was reduced by an order of magnitude in order to show how it scales the overall calculation of the discrete maximum principle. The results are shown in Figures 2 through 4 with the following definition for each case:

Run	Modified Term	Modification
All Terms	None	None
Case 0	$\int_0^\infty 2\pi B_u \frac{\sigma_0}{\Sigma} \left( \frac{1}{2} - E_3(\hat{\Sigma}\Delta_x) \right) d\nu$	$\rightarrow 0$
Case 1	$\frac{\sigma_p}{\lambda^2} L \frac{1}{\Sigma} \left( \frac{1}{2} - E_3(\hat{\Sigma}\Delta_x) \right)$	$\div 10$
Case 2	$\frac{c_1 \sigma_p}{\lambda \Delta_x} (1 - e^{-\lambda \Delta_x})$	$\rightarrow 0$
Case 3	$\frac{\sigma_p}{\lambda^2} A \Delta_x$	$\rightarrow 0$
Case 4	Term (33d)	$\rightarrow 0$
Case 5	Cases 2, 3, and 4 combined	$\rightarrow 0$

As can be seen, Case 1 had the greatest impact, followed by Case 0, with Case 3 in a distant third place. The terms eliminated in Cases 2 and 4, on the other hand, seem to have very little real impact on the overall location of the maximum principle violations. In order to minimize computation, the terms left out in cases 2 and 4 will be left out of the implementation of the DMP.

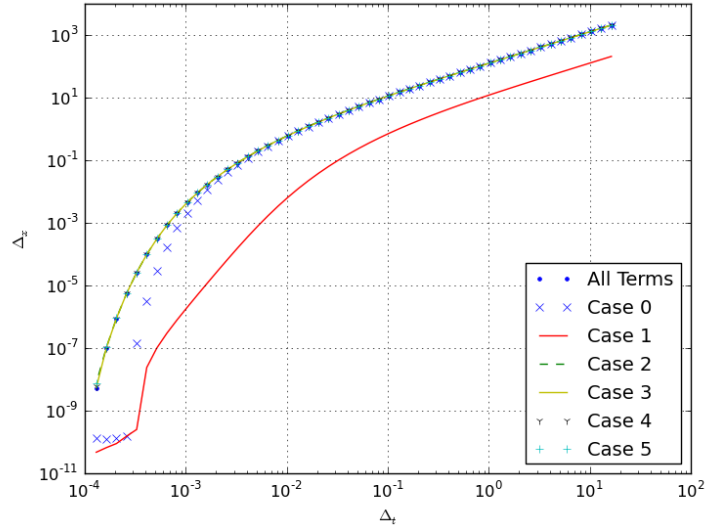
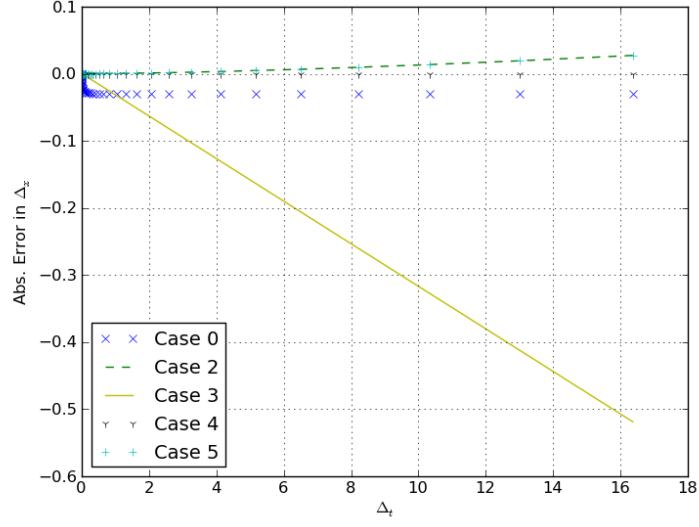
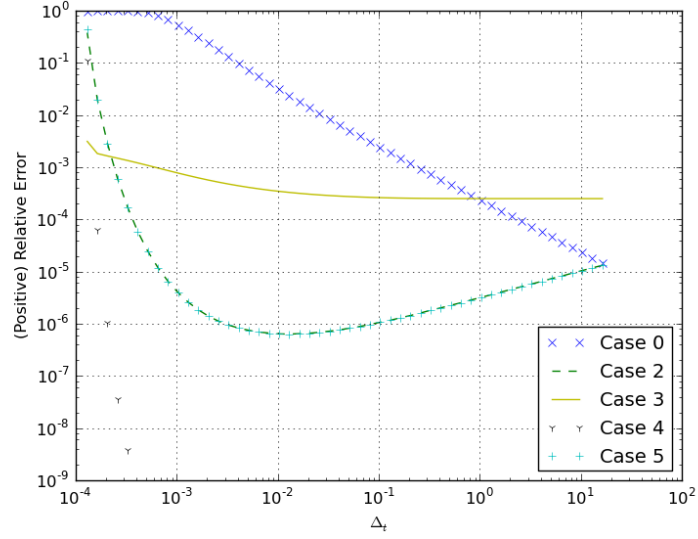


Figure 2: Energy Deposited,  $R$

Figure 3: Absolute Error in  $R$  ApproximationsFigure 4: Relative Error in  $R$  Approximations

Removing the two least-significant terms in  $R$ , we can rearrange to get

$$\tilde{R} \simeq \frac{f_0 \Delta_t}{\Delta_x} \left( \zeta - \frac{\sigma_p}{\lambda^2} \tilde{A} \Delta_x - \frac{\sigma_p}{\lambda^2} \frac{1 - f_0}{-D} \zeta \right), \quad (35)$$

where we define the uncollided flux integral

$$\zeta \equiv \int_0^\infty 2\pi\sigma_0 B_u \left[ \frac{1}{2} - E_3(\hat{\Sigma}\Delta_x) \right] d\nu. \quad (36)$$

### 3.4 Multiple Gradients

Thus far we have assumed a one-dimensional problem with a Marshak boundary on the left and a generally uninteresting right boundary condition. This allowed us to assume only steep temperature gradients on one side of the left boundary cell during the first time step. We now desire to apply the DMP in general to each cell in the mesh, so that an inequality similar to Eq. (32) can be computed for a cell with steep temperature gradients on multiple sides. We will do this by accounting for impingent radiation on multiple faces of a cell in our approximation of  $\tilde{R}$ , although we will continue to treat the radiation as being isotropic and Planckian. The primary result of the Marshak boundary assumption allowed us to find the solution in Eq. (23). This was then used to calculate the uncollided scalar intensity  $\hat{\phi}_0$ . In the 1D case,  $\hat{\phi}_0$  can be restated as follows:

$$\hat{\phi}_1 \equiv \int_{-1}^1 \hat{I}_i d\mu = \int_{-1}^0 \hat{I}_i d\mu + \int_0^1 \hat{I}_i d\mu. \quad (37)$$

Because the initial conditions prescribe no uncollided intensity in a cell initially, the intensity present at a point  $x$  can only originate from incident intensity on the boundaries. The differential equation describing this is given in Eq. (22) and is solved in Eq. (23). There is physical meaning to the terms:  $2\pi B_u$  represents the initial spectrum of intensity found at the Marshak boundary entering the cell, and  $e^{-\Sigma x/\mu}$  attenuates this intensity through material interactions up to point  $x$ . Hence,

a similar expression for uncollided flux arriving at  $x$  from the right boundary can be derived as well.

Let  $B_L$  replace  $B_u$  as the Planck radiation spectrum on the left boundary, and let  $B_R$  represent a similar spectrum on the right boundary. Similarly let  $\hat{I}_{L,i}$  and  $\hat{I}_{R,i}$  represent the incident uncollided intensity at the left and right right boundary, respectively. Eq. (24) becomes

$$\begin{aligned}\hat{\phi}_1 &\equiv \int_{-1}^1 \hat{I}_i d\mu, \\ &= \int_{-1}^0 \hat{I}_{R,i} d\mu + \int_0^1 \hat{I}_{L,i} d\mu, \\ &= \int_{-1}^0 \hat{I}_{R,i} d\mu + \int_0^1 2\pi B_L e^{-\hat{\Sigma}x/\mu} d\mu.\end{aligned}\tag{38}$$

Because of the arbitrary definition of positive  $\mu$ , we expect  $\hat{I}_{R,i}$  to have a similar form to  $\hat{I}_{L,i}$ . However, the attenuation term must be treated differently for negative  $\mu$  radiation. Because the radiation enters at the right and moves to the left, the attenuation distance for the right side becomes  $\Delta_x - x$ . Thus by inspection and symmetry,

$$\int_{-1}^0 \hat{I}_{R,i} d\mu = \int_{-1}^0 2\pi B_R e^{-\hat{\Sigma}(\Delta_x - x)/\mu} d\mu.\tag{39}$$

To continue shaping this new first term to correlate with the second term, consider that in the first integral all values of  $\mu$  are negative. Given this condition,

$$\mu = -|\mu|, \quad \mu \leq 0.$$

Substituting this into Eq. (39) and making a change of integration variable to  $|\mu|$ , we obtain an expression very similar to the second term in Eq. (38):

$$\int_{-1}^0 \hat{I}_{R,i} d\mu = \int_0^1 2\pi B_R e^{-\hat{\Sigma}(x - \Delta_x)/|\mu|} d|\mu|.\tag{40}$$



Since the new attenuation coefficient is identical in form to that in Eq. (23), the integral solution has the same form. Thus,

$$\hat{\phi}_1 = 2\pi B_L E_2(\hat{\Sigma}x) + 2\pi B_R E_2\left(\hat{\Sigma}(\Delta_x - x)\right) \quad (41)$$

Eq. (41) is sufficiently different from Eq. (23) that the original operator  $L$  is divided into an operator  $L_L$  for the left side and  $L_R$  for the right:

$$L_L(\xi) \equiv \frac{1-f_0}{-D} \int_0^\infty \sigma_0 2\pi B_L \xi \, d\nu, \quad (42a)$$

$$L_R(\xi) \equiv \frac{1-f_0}{-D} \int_0^\infty \sigma_0 2\pi B_R \xi \, d\nu, \quad (42b)$$

which, using the same procedure as in [13], leads to a new particular solution for  $\check{\phi}_1$ :

$$\begin{aligned} \check{\phi}_1^p = \frac{1}{\lambda^2} \Bigg[ & -A - L_R E_2(\hat{\Sigma}(x - \Delta_x)) + L_R \frac{\hat{\Sigma}}{2\lambda} \left( e^{-\lambda x} g(x - \Delta_x) + e^{\lambda x} E_1[(\lambda + \hat{\Sigma})(\hat{\Sigma}(x - \Delta_x))] \right) \\ & - L_L E_2(\hat{\Sigma}x) + L_L \frac{\hat{\Sigma}}{2\lambda} \left( e^{-\lambda x} g(x) + e^{\lambda x} E_1[(\lambda + \hat{\Sigma})x] \right) \Bigg], \end{aligned} \quad (43)$$

where

$$g(x) \equiv \int \frac{e^{(\lambda - \hat{\Sigma})x}}{x} dx = \begin{cases} \text{Ei}[(\lambda - \hat{\Sigma})x], & \lambda \neq \hat{\Sigma}, \\ \ln x, & \lambda = \hat{\Sigma}, \end{cases} \quad (44)$$

which makes use of the extension to  $\text{Ei}(x)$  noted in [1]:

$$\text{Ei}(-x) \equiv -E_1(x), \quad 0 < x.$$

Next we apply the Marshak and finite boundary conditions. The homogeneous solution for  $\check{\phi}_1$  is the same as derived earlier, and we still set  $c_2 = 0$  to preserve the condition in Eq. (30c). After some algebraic manipulation, and noting the convenient equal divergence and limits described in [13], it can be shown that the

average energy deposited in a cell ( $\tilde{R}$ ) follows the superposition principle for left and right sides of the cell. That is to say,

$$\tilde{R} = \tilde{R}_L + \tilde{R}_R.$$

The temperature update in a cell then becomes

$$\begin{aligned} \frac{c_v}{\Delta_t}(T_1 - T_0) + f_0 c \sigma_p a T_0^4 &= \tilde{R}_L + \tilde{R}_R, \\ T_1 - T_0 &= \frac{\Delta_t}{c_v}(\tilde{R}_L + \tilde{R}_R - f_0 c \sigma_p a T_0^4). \end{aligned} \quad (45)$$

Two separate equations fall out of Eq. (45), one for each side of the cell. Since both the left boundary temperature  $T_L$  and the right boundary temperature  $T_R$  limit the time step in similar ways, we here define the maximum temperature

$$T_m \equiv \max(T_L, T_R).$$

$$T_m - T_1 = T_m - T_0 - \frac{\Delta_t}{c_v}(\tilde{R}_L + \tilde{R}_R - f_0 c \sigma_p a T_0^4), \quad (46)$$

As in [13], the maximum principle is only satisfied if the boundary temperature is greater than the update temperature, meaning the right side of Eq. (46) is positive:

$$T_m - T_0 > \frac{\Delta_t}{c_v}(\tilde{R}_L + \tilde{R}_R - f_0 c \sigma_p a T_0^4), \quad (47)$$

or, rearranging, the maximum principle can be stated in the same form as that in [13],

$$\Delta_t < \frac{c_v(T_m - T_0)}{\tilde{R}_L(\Delta_x, \Delta_t) + \tilde{R}_R(\Delta_x, \Delta_t) - f_0 c \sigma_p a T_0^4}, \quad (48)$$

It should be noted that the term  $T_m - T_0$  in the numerator here is misleading. An analysis of the frequency-independent DMP leads to an inequality with  $T_m^4 - T_0^4$  in the denominator, for example.

### 3.5 Multidimensional Considerations

Given the results achieved in the one-dimensional case, the maximum principle in multiple dimensions can be extrapolated by adjusting  $\tilde{R}$ . Since the average energy deposited ( $\tilde{R}$ ) is separable in that it follows superposition rules, the composite term is as follows:

$$\tilde{R}_{tot} = \sum_{s=1}^S \tilde{R}_s(\Delta_x, \Delta_t), \quad (49)$$

where  $S$  is the number of faces on the cell in question and  $s$  represents one of those faces.

The question of what to use for  $\Delta_x$ , the spatial discretization, in higher dimensions is a valid one, and needs addressing. In one dimension, it is obvious that the cell size is equal to its length. However, in multiple dimensions, the cell size is an area or volume, and linear distance becomes more difficult to define uniquely. To resolve this, we turn to the work done by Bardsley and Dubi [2], who expound the average-chord-length theorem developed by Dirac [3]. This theorem states that for any three-dimensional volume, the average chord length within that volume is given by

$$\bar{\Delta}_x = 4 \frac{V}{A}, \quad (50)$$

where  $V$  is the volume and  $A$  is the surface area of the volume. We use this definition to describe the value  $\Delta_x$  in three dimensions to redefine the discrete maximum inequality

$$\Delta_t < \frac{c_v(T_m - T_0)}{\tilde{R}_{tot}(\Delta_x, \Delta_t) - f_0 c \sigma_p a T_0^4}, \quad T_m = \max(T_s). \quad (51)$$

### 3.6 Multigroup Frequencies

A “multigroup approximation” is often performed to allow the emission and absorption characteristics of individual energy spectra to be represented as a sum instead of a continuous integral. We derive such a technique here. Without making any approximation, the integrated value of a general function  $f(\nu)$  can be represented as

$$\int_0^\infty f(\nu) d\nu = \sum_{\nu=0}^\infty f(\nu).$$

We can further split this continuous sum into groups of continuous sums, still without making any approximations:

$$\int_0^\infty f(\nu) d\nu = \sum_{g=0}^\infty f_g,$$

where the group function is defined

$$f_g \equiv \int_g^{g-1} f(\nu) d\nu.$$

Note here that lower values of  $g$  correspond to higher values of  $\nu$ . as is the typical convention in multigroup theory.

Since finding the integrated value of  $f(\nu)$  is still no easier than before, we now make an approximation by truncating the infinite sum:

$$\int_0^\infty f(\nu) d\nu \approx \sum_{g=0}^G f_g.$$

In the limit that  $G \rightarrow \infty$ , there is no approximation made.

As necessary, further approximation can be made if  $f(\nu)$  is separable into several functions of  $\nu$ . For example, let

$$f(\nu) = \frac{A(\nu)B(\nu)}{C(\nu)}.$$

In the multigroup approximation, then,

$$\int_0^\infty f(\nu) \approx \sum_{g=0}^G f_g = \sum_{g=0}^G \frac{A_g B_g}{C_g}.$$

This is an approximation in that, for the general case,

$$\int \frac{A(x)B(x)}{C(x)} dx \neq \frac{\int A(x) dx \int B(x) dx}{\int C(x) dx}.$$

However, using these multigroup approximations, previously-inhibiting integrations can be discretized into terms that can be computed.

### 3.6.1 *Riemann Approximation*

In this work, a Riemann approximation is used to find the group values for continuous integrals as described above. The basic tenet of this approximation is that continuous integrals may be approximated as the sum of many trapezoidal figures that roughly approximate the shape of the integrand (see Figure 5). There are several different methods of implementing the Riemann sum. The value of the function over a range can be the function evaluated at the leftmost part of the range, the value at the rightmost part of the range, or the value in the center of the range. The approximation in Figure 5 is representative of a fourth, more accurate method: the “trapezoidal” method. In this method, the Riemann segment an upper value that is the linear-fit average of the function in the cell instead of the function evaluated at any one point. For this method, the integral of the function is approximated as

$$\int_a^b f(x) dx \approx \sum_{r=1}^R \frac{[f(x_r) + f(x_{r+1})] \Delta r}{2}$$

where  $x_r$  is the value of  $x$  at the leftmost bound of the Riemann segment.

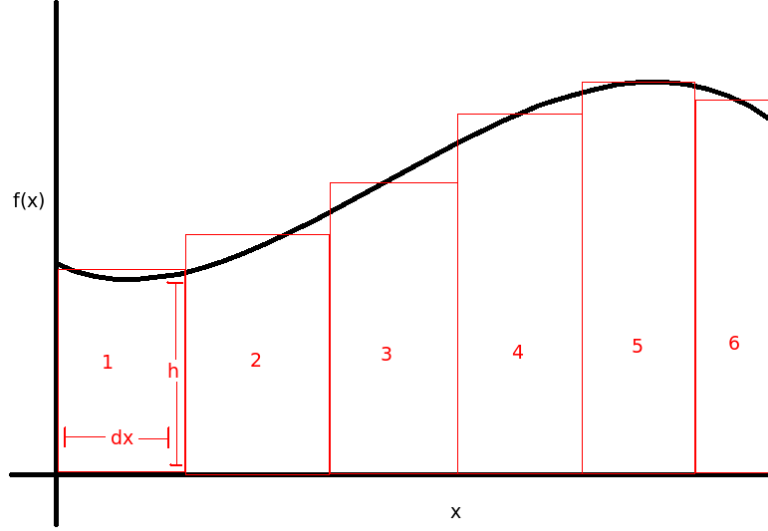


Figure 5: Visualization of Riemann Sum Method

### 3.6.2 Accuracy of Multigroup Approximation

In order to compare the multigroup approximation to a more analytic solution, the DMP was calculated using the multigroup method described above, then with an analytic solve using the **MatLab** computer algebra software. The results are shown in Figure 6. Calculating the relative error between the two methods led to a machine-precision difference in all cases. For the large set of runs used to create the discrete maximum curve shown in Figure 6, the analytic method took about 160 seconds, while the multigroup method took just over 23 seconds, suggesting the multigroup method is on the order of seven times faster to calculate than the analytic method.

Using this multigroup approximation technique and the numerical solution for  $E_3(\hat{\Sigma}\Delta_x)$  discussed in Appendix ??, Eq. (35) becomes computationally straightforward.

An interesting result occurs when the multigroup approximation is applied to

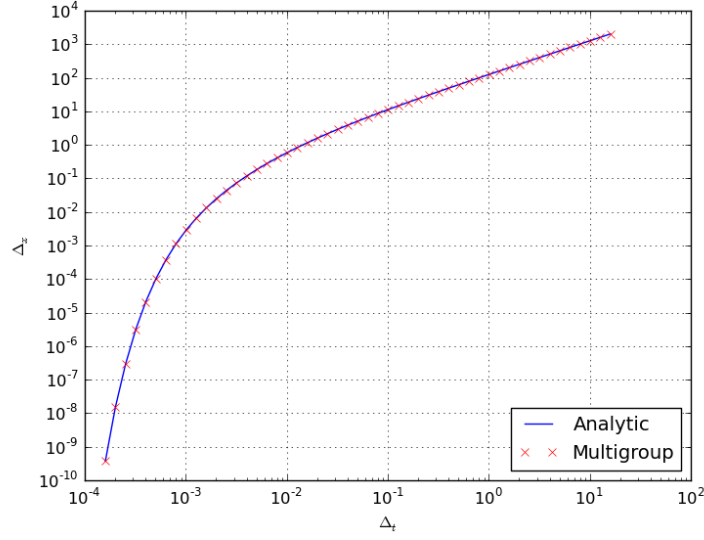


Figure 6: Multigroup versus Analytic Solutions for the DMP

the estimate  $\tilde{R}$ . In Figure ?? we note that the analytic Discrete Maximum Principle curve, obtained from a numerical integral over frequency in `Matlab`, diverges from the experimental data somewhere between  $\Delta_t$  of 0.001 and 0.01 shakes. This suggests that the analytic discrete maximum principle is not conservative enough to match experiment. However, when the multigroup approximation is applied, the curve matches much more closely, as shown in Figure 7. It is not entirely surprising that the multigroup approximation is more accurate, since the experimental results were generated using a 100-group frequency grid in IMC use code `milagro`.

### 3.6.3 Grey Case

Because of the structure of the use codes that the DMP will likely be used in, we deem it essential to construct an algorithm that will handle the 1-group gray case as well as the multifrequency case. A derivation of the discrete maximum principle for the frequency-independent gray case is derived here that takes the same form as Eq. (32).

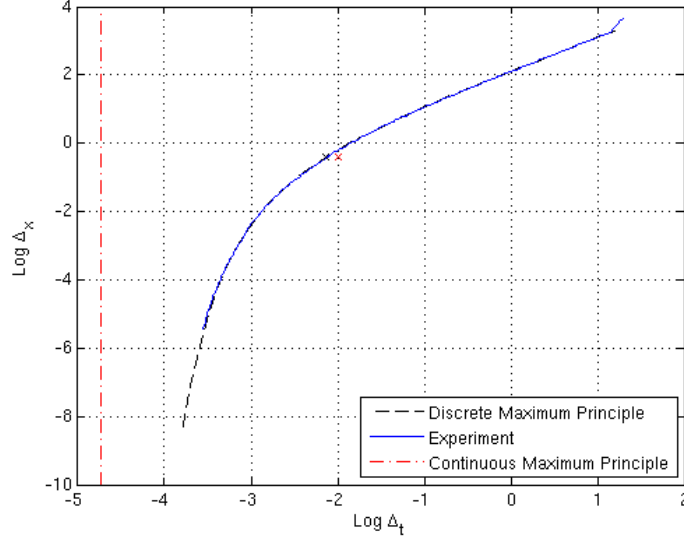


Figure 7: Multigroup Approximation of DMP

We start with the gray transport equation in one dimension in [4], which assumes that frequency is independent of angle and can be integrated out:

$$\frac{1}{c} \frac{\partial I}{\partial t} + \mu \frac{\partial I}{\partial x} + \sigma_0 I = \sigma_0 (1 - f_0) \frac{1}{2} \int_{-1}^1 I \, d\mu + \sigma_0 f_0 \frac{acT_0^4}{2}, \quad (52)$$

with the boundary and initial conditions

$$I(0, \mu, t) = \frac{ac}{2} T_u^4 \equiv B_u, \quad 0 < \mu \leq 1, 0 \leq t, \quad (53)$$

$$I(X, \mu, t) = \frac{ac}{2} T_0^4 \equiv B_0, \quad -1 < \mu \leq 0, 0 \leq t, \quad (54)$$

$$I(x, \mu, 0) = \frac{ac}{2} T_R^4 \equiv B_R, \quad 0 \leq x \leq \infty, |\mu| < 1. \quad (55)$$

Implicitly time differencing Eq. (52), we arrive at

$$\frac{1}{c} \frac{I_1 - I_0}{\Delta_t} + \mu \frac{\partial I_1}{\partial x} + \sigma_0 I_1 = \sigma_0 (1 - f_0) \frac{1}{2} \int_{-1}^1 I_1 \, d\mu + \sigma_0 f_0 \frac{acT_0^4}{2}, \quad (56)$$

where  $I_1 \equiv I(t_1)$ . Using the initial condition in Eq. (55),

$$\mu \frac{\partial I_1}{\partial x} + \Sigma_t I_1 = \frac{\Sigma_t - \Sigma_a}{2} \int_{-1}^1 I_1 \, d\mu + A, \quad (57)$$



where

$$\Sigma_t \equiv \sigma_0 + \frac{1}{c\Delta_t},$$

$$\Sigma_a \equiv f_0\sigma_0 + \frac{1}{c\Delta_t},$$

$$A \equiv \frac{ac}{2} \left( f_0\sigma_0 T_0^4 + \frac{T_R^4}{c\Delta_t} \right).$$

Next a diffusion approximation is applied. Defining  $\phi \equiv \int I_1 d\mu$  and  $D \equiv 1/3\Sigma_t$ ,

$$-D \frac{\partial^2 \phi}{\partial x^2} + \Sigma_a \phi = A, \quad (58)$$

and we apply the Marshak boundary condition

$$\phi(0) - 2D \frac{\partial \phi}{\partial x} \Big|_{x=0} = 2B_u.$$

The solution to this set of differential equations is

$$\phi(x) = \frac{A}{\Sigma_a} + \frac{2B_u - 2A/\Sigma_a}{1 + 2\sqrt{\frac{\Sigma_a}{3\Sigma_t}}} e^{-x\sqrt{3\Sigma_a\Sigma_t}}. \quad (59)$$

We next use this in the temperature update equation applied to the first cell,

$$\frac{c_v}{\Delta_t}(T_1 - T_0) = f_0\sigma_0 \left( \frac{1}{\Delta_x} \int_0^{\Delta_x} \phi(x) dx - acT_0^4 \right).$$

Applying Eq. (59), then, and rearranging,

$$T_u - T_1 = T_u - T_0 - \Delta_t \frac{\sigma_0 f_0}{c_v} \left[ \frac{A}{\Sigma_a} + \left( \frac{2}{B_u} - 2A/\Sigma_a \right) \frac{1}{\Lambda} \right], \quad (60)$$

where we define  $\Lambda$  by

$$\Lambda \equiv \left( 1 + 2\sqrt{\frac{\Sigma_a}{3\Sigma_t}} \right) \left( \frac{\Delta_x \sqrt{3\Sigma_a\Sigma_t}}{1 - e^{-\Delta_x \sqrt{3\Sigma_a\Sigma_t}}} \right).$$

Requiring that the left side of Eq. (60) remain positive, a gray discrete maximum principle can be derived in a form similar to the multigroup one:

$$\Delta_t < \frac{c_v(T_u - T_0)}{R - f_0 c \sigma_0 a T_0^4}, \quad (61)$$

with

$$R \equiv \frac{f_0 \sigma_0 A}{\Sigma_a} + f_0 \sigma_0 \left( 2B_u - \frac{A}{\Sigma_a} \right) \frac{1}{\Lambda}.$$

Ideally, the multifrequency formulation in the case that  $G = 1$  should return identical results to the gray case; however, we expect some small deviation in the two solutions because of the uncollided flux distribution assumptions used in the multifrequency case. It is expected, however, that these discrepancies are negligible. It should also be noted that in the gray case,  $\sigma_0 = \sigma_p$ .

### 3.7 Summary

Having removed the assumption of initial material and radiation thermal equilibrium, truncated the estimate of energy deposited  $\tilde{R}$ , allowed for multiple “hot” cells in predicting DMP violations, and applied multigroup frequency approximations, we arrive at the adjusted DMP, with the following definitions:

$$\Delta_t < \frac{c_v(T_m - T_0)}{\tilde{R}_{tot}(\Delta_x, \Delta_t) - f_0 c \sigma_p a T_0^4}, \quad T_m = \max(T_s), \quad (62a)$$

$$\tilde{R}_{tot}(\Delta_x, \Delta_t) \equiv \sum_{s=1}^S \tilde{R}_s(\Delta_x, \Delta_t), \quad (62b)$$

$$\tilde{R}_s(\Delta_x, \Delta_t) = \frac{f_0 \Delta_t}{\Delta_x} \left( \zeta - \frac{\sigma_p}{\lambda^2} \tilde{A} \Delta_x - \frac{\sigma_p}{\lambda^2} \frac{1 - f_0}{-D} \zeta \right), \quad (62c)$$

$$\zeta \equiv \sum_{g=0}^G 2\pi \sigma_{0,g} B_{u,g} \left[ \frac{1}{2} - E_{3,g}(\hat{\Sigma}_g \Delta_x) \right], \quad (62d)$$

$$\tilde{A} \equiv -\frac{acT_R^4}{c\Delta_t D} - \frac{f_0 \sigma_p}{D} acT_0^4. \quad (62e)$$

Eqs. (62) represent the adjustments of this work to the discrete maximum principle.

## 4 Results

### 4.1 Introduction

This chapter contains TODO

### 4.2 Multigroup Treatment

This section evaluates the effectiveness of the multigroup treatment of the DMP. In order to verify the accuracy of the multigroup treatment, we compare predicted maximum principle violations to actual violations on the same problem benchmarked in [13]. This problem is a one-dimensional Marshak wave, with a constant hot source on one side and an initially cold material. For a variety of time step sizes  $\Delta_t$ , several grid spacings  $\Delta_x$  are selected and the first time step is solved and a check is performed for a maximum principle violation in the first cell, which is the limiting  $\Delta_x$  and  $\Delta_t$  for boundedness. The smallest  $\Delta_x$  which produces a maximum principle violation is noted. The data set of these minimum violating  $\Delta_x$  and corresponding  $\Delta_t$  yields the bounding  $\Delta_t$  and  $\Delta_x$  set for this particular problem.

Parallel to the development of the DMP bounds, each problem solution also predicts violations using the DMP algorithm. The predicted bounds are a set of minimum  $\Delta_x$  that *predict* a DMP violation for each  $\Delta_t$ . The success of the DMP algorithm is determined by how close the predicted violations match the actual violations.

In order to show the contrast between actual violations and predicted violations,

a color and symbol scheme is used in Figure 8. A “plus” mark denotes a successful prediction by the DMP algorithm, while a failed prediction is indicated by a filled circle. A red mark is an actual maximum principle violation, while a black mark is bounded.

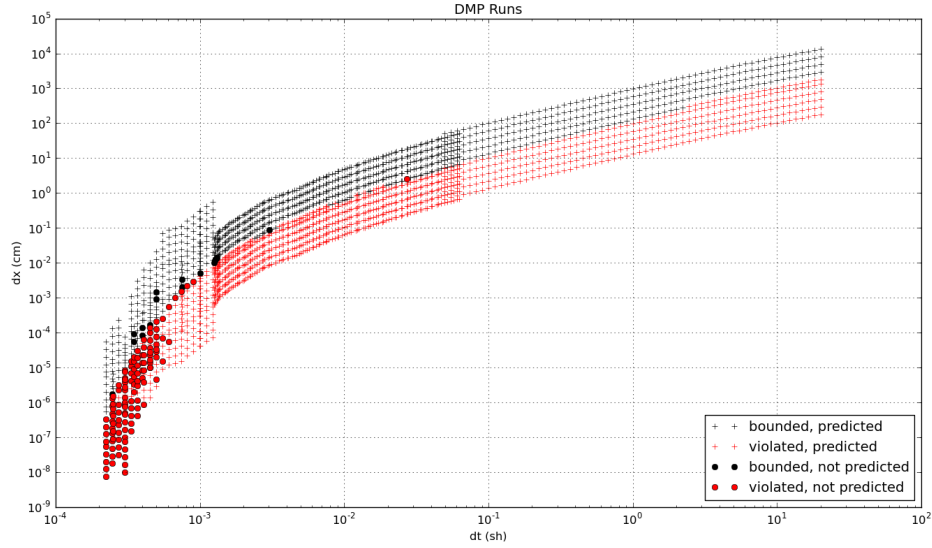


Figure 8: Marshak Wave in One Dimension

For larger  $\Delta_t$  and  $\Delta_x$ , the DMP algorithm very accurately predicts maximum principle violations. This accuracy diminishes with decreasing  $\Delta_t$ , however. Recalling the truncation approximation made to the estimated energy deposited in a cell over a time step ( $\tilde{R}$ ), the relative error introduced by the approximation increased significantly as  $\Delta_t$  is less than about 0.001 shakes. This leads us to expect a poorer performance by the DMP as the time step nears  $10^{-4}$  shakes, evident here. To verify this failure of the DMP algorithm is due to truncation terms, we test the pseudo-analytic DMP from [13] and its truncation for several of the incorrect DMP runs in Fig. 8. If the pseudo-analytic DMP with no truncation of  $\tilde{R}$  correctly predicts maximum principle violations while the truncated DMP does not,

this provides strong suggestion that truncation is the leading effect in the DMP poor performance for small  $\Delta_x$ .

TODO

### 4.3 Non-Equilibrium Conditions

In this section we explore non-equilibrium conditions where the radiation temperature and material temperature are not equal at the beginning of a time step. Physically this could occur when a small, thin material is bombarded by high-energy photons, where the temperature of the radiation field is substantially higher than the heat of the material for some time. TODO

### 4.4 Multiple Sources

We now turn to considering a multidimensional case with hot sources on two neighboring sides of a material. In particular, we address a problem with a choice of  $\Delta_t$  and  $\Delta_x$  such that neither surface source causes a maximum principle violation by itself, but when combined overheating occurs. This tests the linear superposition assumption for estimated energy deposition.

### 4.5 Small $\Delta T$

An unexpected discovery about the characteristics of the DMP emerged while observing multiple time steps as a Marshak wave distributes across the material. The DMP was used to predict violations on each cell of the mesh. To avoid division-

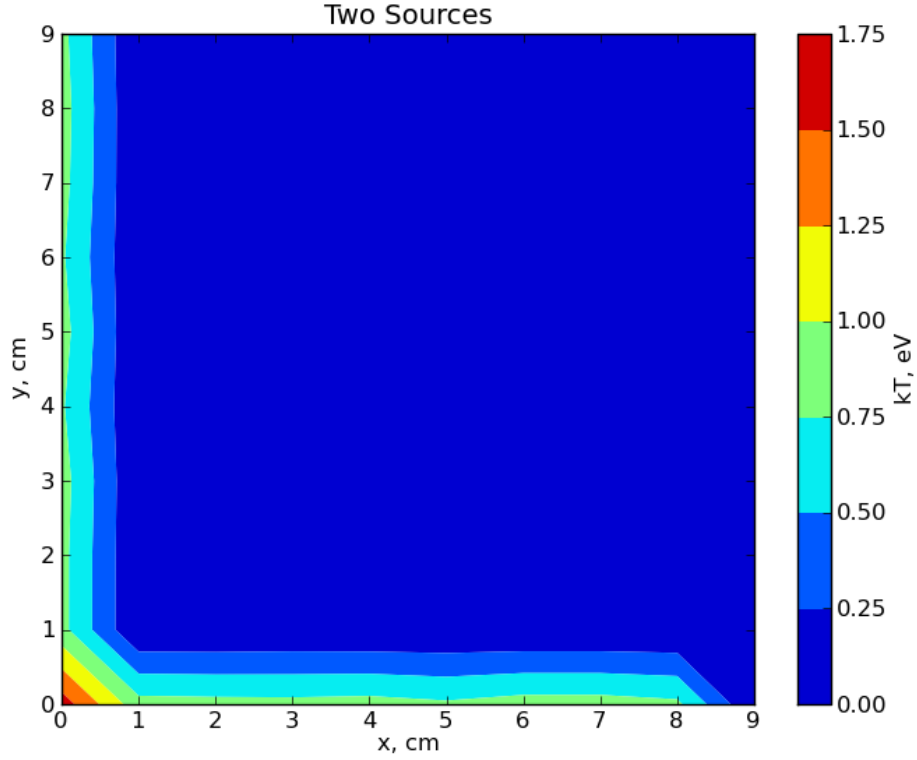


Figure 9: Multiple Marshak Wave Sources

by-zero errors, if the estimated energy to be deposited in a cell  $\tilde{R}$  is zero for all cells near the one being evaluated, the DMP assumed no violations from that cell. During the first time step, then, only the first cell is checked for DMP violations for a 1D Marshak wave problem. In successive steps, however, the DMP incorrectly predicted maximum principle violations in cells where neighbor cell temperatures were very close to the cell's own temperature. As it has been implemented to this point, this is a significant flaw in the implementation of the DMP and deserves significant attention. For now, we demonstrate the following using the grey case DMP inequality to show how these false predictions come about.

The grey, one-dimensional DMP inequality is as follows: TODO reference ear-

lier derivation

$$\Delta_t < \frac{c_v}{\sigma ac} \frac{1}{\frac{T_u^4 - T_0^4}{T_u - T_0} \frac{1}{\Lambda} - 4\alpha T_0^3}. \quad (63)$$

We can represent a neighbor cell temperature  $T_u$  that is higher than the local cell temperature  $T_0$  as the cell temperature plus some difference in temperatures, or

$$T_u = T_0 + \Delta T. \quad (64)$$

Noting the fourth-order terms in Eq. 63, we consider

$$T_u^4 = T_0^4 + 4\Delta T T_0^3 + 6\Delta T^2 T_0^2 + 4\Delta T^3 T_0 + \Delta T^4, \quad (65)$$

or, as  $\Delta T \rightarrow 0$ , which is the case of interest here,

$$T_u^4 = T_0^4 + 4\Delta T T_0^3 + 6\Delta T^2 T_0^2 + \mathcal{O}(\Delta T^3). \quad (66)$$

Inserting Eqs. 64 and 66 into Eq. 63,

$$\Delta_t < \frac{c_v}{\sigma ac} \frac{\Lambda}{4T_0^3(1 - \Lambda\alpha) + 6\Delta T T_0^3 + \mathcal{O}(\Delta T^2)}. \quad (67)$$

If  $\Lambda$  were strictly less than unity, this would not pose a problem; however, in many limiting cases TODO,  $\Lambda > 1$ , which, for small  $\Delta T$ , results in the DMP requiring a negative time step in order to satisfy the inequality. Rearranging, this leads to a litmus test for applying the DMP; that is, if

$$\Delta T \leq \frac{2}{3}(\Lambda\alpha - 1)T_0, \quad (68)$$

the DMP will be an inaccurate predictor of maximum principle violations. Fortunately, since this limit is only of concern when  $\Delta T$  is small, and overheating only occurs when  $\Delta T$  is large, this test should restore accuracy to the DMP algorithm.

A similar result for the multifrequency case is a desirable pursuit for the future.

TODO move this derivation into the methods section

In Figs. 10 and 11, the benefit of the switch is demonstrated. Black dots indicate a maximum principle violation prediction, and black crosses show where the DMP predicts no violation.

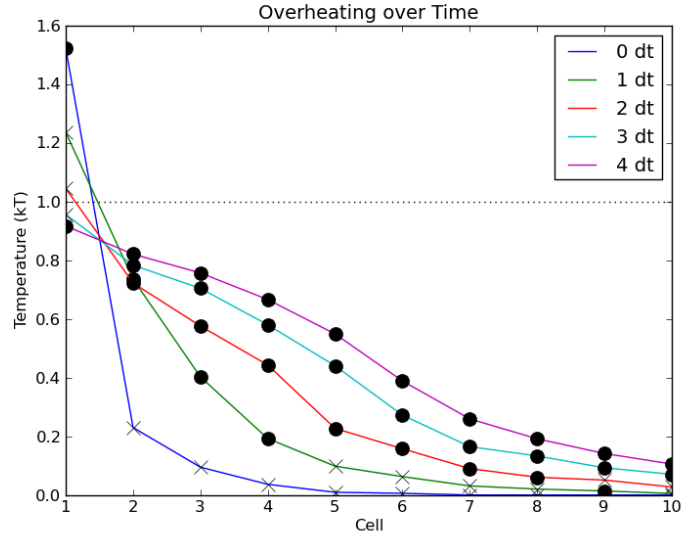


Figure 10: Multiple Time Steps, Before Switch

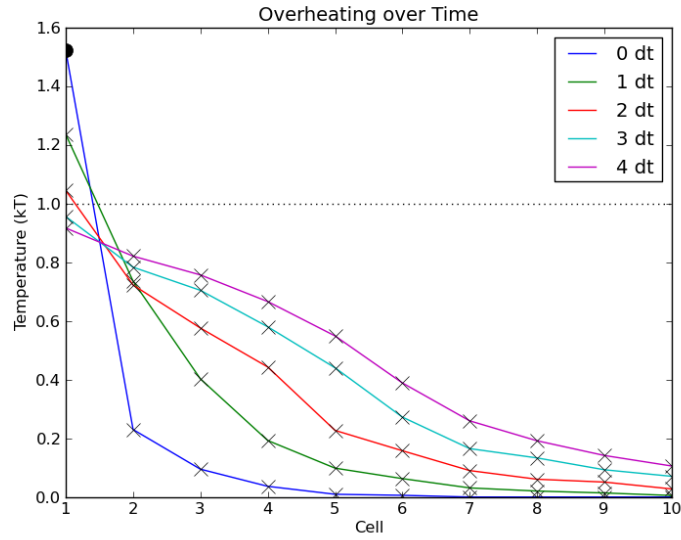


Figure 11: Multiple Time Steps, After Switch



## 4.6 Summary

TODO

## 5 Conclusions

### 5.1 Future Work

There is still significant work that can be done to develop the discrete maximum principle and its applications in IMC radiative heat transfer codes. In particular, the next logical implementation step is to build a routine whereby the user is given an appropriate time step for the problem and choice of spatial step when a violation is predicted. Unfortunately, the limiting time step is dependent on the estimated energy deposited in the cell, which in turn is dependent on time step itself, so an iterative procedure would be necessary, although I expect a simple Euler method could be used to swiftly find such a time step for the most limiting cell in the problem.

Additionally, work is ongoing with Dr. Wollaber at Los Alamos National Laboratory to determine necessary and sufficient conditions to bound the discrete maximum principle in a somewhat more robust way than has been done here. As of this writing, a necessary condition has been determined using a purely absorbing (time step approaches zero and Fleck factor approaches unity) scheme; however, the sufficient purely scattering (time step approaches zero and Fleck factor approaches zero) is very difficult to analyze analytically [?].

Associated work is also ongoing to use partial Monte Carlo runs at each time step to increase the implicitness of the solution method. In particular, work performed by Alex Long in association with Lawrence Livermore National Laboratory has shown the overheating event can be diminished using this increasingly implicit methodology. It would be significant to investigate using this updated information

to adjust the discrete maximum principle limit as well; however, since this update step decreases the severity of the limit, it is likely the run would be flagged as a likely violation before the update step, so some consideration would be necessary to determine the best way to implement this improved check.

**\*\*TODO other future work?**

## Bibliography

- [1] M. Abramowitz and I. A. Stegun, *Handbook of mathematical functions with formulas, graphs, and mathematical tables*, Dover Publications, Inc., New York, 1972.
- [2] J. N. Bardlsey and A. Dubi, *Average transport path length in scattering media*, SIAM Journal on Applied Mathematics **40** (1981), 71–77.
- [3] P. A. M. Dirac, *Approximate rate of neutron multiplication for a solid of arbitrary shape and density*, Declassified British Report MS-D-5, Part I (1943).
- [4] J. A. Fleck and J. D. Cummings, *An Implicit Monte Carlo Scheme for Calculating Time and Frequency Dependent Nonlinear Radiation Transport*, J. Comp. Phys. **8** (1971), 313–342.
- [5] Jr. J A Fleck, *The calculation of nonlinear radiation transport by a monte carlo method*, Computational Methods in the Physical Sciences **1** (1963), 43.
- [6] E. W. Larsen J. D. Densmore, *Asymptotic equilibrium diffusion analysis of time-dependent monte carlo methods for grey radiative transfer*, J. Comp. Phys. **199** (2004), 175–204.
- [7] T. M. Evans M. W. Buksas J. D. Densmore, T. J. Urbatsch, *A hybrid transport-diffusion method for monte carlo radiative-transfer simulations*, J. Comp. Phys. **222** (2007), 485–503.
- [8] C. A. Forest L. L. Carter, *Nonlinear radiation transport simulation with an implicit monte carlo method*, Tech. Rep. LA-5038, Los Alamos National Laboratory (1973).
- [9] Edward W. Larsen and Bertrand Mercier, *Analysis of a Monte Carlo method for nonlinear radiative transfer*, J. Comp. Phys. **71** (1987), 50–64.
- [10] A. Long, *Todo*, MS Thesis, Oregon State University (2012).
- [11] T. N’kaoua, *Solution of the nonlinear radiative transfer equations by a fully implicit matrix monte carlo method coupled with the rosseland diffusion equation via domain decomposition*, SIAM J. Sci. Stat. Comput. **12** (1991), 505.
- [12] A. B. Wollaber, *Advanced monte carlo methods for thermal radiation transport*, Ph.D. Thesis, University of Michigan (2008).
- [13] Allan B. Wollaber, Edward W. Larsen, and Jeffery D. Densmore, *Towards a frequency-dependent discrete maximum principle for the Implicit Monte Carlo equations*, Proc. of ANS M&C 2011, May 8-12, 2011.